Estimating Radiation Exposure through Ray Tracing Simulation

Elisa Foderaro[1], Rosanna Greco[1] and Giorgio De Magistris[1]

[1]Department of Computer, Control, and Management Engineering of Sapienza University of Rome, Italy

Abstract

Radiation plays a critical role in modern medical diagnostics and treatments but poses significant risks to healthcare personnel. Traditional dose estimation methods, primarily based on dosimeters placed on selected body parts, neglect the varying radiosensitivity of different organs. In this work, we present a system that models effective radiation dose by simulating three-dimensional (3D) environments including radiation sources, shielding objects, and human models segmented by MeshCNN. We employed a ray tracing algorithm to simulate radiation behavior, considering both spatial attenuation (via inverse square law) and material shielding (via the Lambert–Beer law). Our approach allows for detailed analysis of organ-specific exposures and the impact of environmental shielding. Results demonstrate the feasibility of using 3D simulation and ray tracing to achieve a more comprehensive and accurate estimation of effective radiation dose in medical environments.

Keywords

ray tracing, radiation dosimetry, medical imaging, mesh segmentation, Monte Carlo methods, 3D modeling

1. Introduction

Radiation is widely utilized in the medical field for both diagnostic and therapeutic purposes. Despite its clinical benefits, radiation exposure poses significant health risks to medical personnel, especially those working in environments where frequent or prolonged exposure occurs. Effective radiation protection strategies are thus essential to mitigate these risks.

Radiation can be classified into particle radiation (e.g., alpha and beta particles) and electromagnetic radiation (e.g., gamma rays and X-rays). While alpha and beta particles have limited penetration abilities, gamma rays and X-rays can deeply penetrate tissues, potentially damaging sensitive organs. Consequently, understanding the behavior of radiation in complex environments and its interaction with the human body is crucial for accurate risk assessment and protection.

In current practice, radiation exposure is typically monitored using personal dosimeters, devices worn on specific body parts to record cumulative doses. However, this method has limitations: it does not account for the varying radiosensitivity of different organs, the shielding effects of surrounding objects, or the spatial distribution of absorbed dose across the body. Moreover, improper usage, calibration issues, and body self-shielding effects can lead to inaccurate estimations.

The absorbed dose, expressed in Gray (Gy), measures the energy deposited per unit mass of tissue but does not reflect the biological impact of different radiation types. To account for this, the equivalent dose (measured in Sievert, Sv) applies a radiation weighting factor. Further, the effective dose incorporates tissue weighting factors, providing a measure of the overall risk by considering the varying sensitivity of different organs.

Exposure to ionizing radiation carries both deterministic and stochastic risks. Deterministic effects, such as skin burns or cataracts, occur above a threshold dose. Stochastic effects, including cancer, have no threshold and their probability increases with dose. The International Commission on Radiological Protection (ICRP) recommends dose limits to protect workers and the general public, emphasizing the ALARA (As Low As Reasonably Achievable) principle.

This work proposes a novel method to estimate the effective dose absorbed by a human body placed in a radiation environment. We designed and implemented a simulation framework that combines 3D modeling, human body segmentation, and ray tracing to simulate radiation propagation and interaction within complex scenes. Using this framework, we can analyze radiation exposure on a per-organ basis, taking into account shielding by environmental objects and self-shielding by body structures.

Our methodology provides a step toward more detailed and realistic radiation exposure assessments, with potential applications in healthcare facilities and radiological safety evaluations.

2. Related works

Nowadays, there is a lot of effort on studying how radiation affects patients [1, 2] and many works attempt to estimate the radiation dose of various medical procedures, such as in [3, 4, 5]. For this type of estimation, most

SYSTEM 2025: 11th Sapienza Yearly Symposium of Technology, Engineering and Mathematics. Rome, June 4-6, 2025

demagistris@diag.uniroma1.it (G. D. Magistris)

of the methods used are based on Monte Carlo (MC) simulation(s), a method extensively used in medical physics applications [6, 7, 8, 9] and considered the *gold standard* thanks to its capability of calculating statistical behavior. In addition to radiation dose estimation, MC techniques are also used for radiotherapy device development [10] and treatment planning [11, 12, 13].

However, the ability to model full particle transport yields high computational complexity which makes MC simulations prohibited for daily clinical practice. To overcome this problem and achieve a fast dose calculation, several Deep Learning frameworks have been developed, e.g. [14, 15, 16].

Although this type of research is interesting, it does not correspond exactly to the objectives of this work. Indeed, we are more interested in the estimation of the effective dose for radiation workers.

The report [17] is better suited for this purpose. However, due to the insufficient data provided by the countries, many of the estimated values are subject to a considerable degree of uncertainty.

Indeed, the current trend is to monitor a person's exposure doses using devices called dosimeters. They rely on numerous physical effects and can be of several types [18]. The most significant for our purposes are:

- Personal dosimeters, used to assess the radiation dose received by an individual who is wearing the device. These are usually small devices worn on the body itself, usually on the torso. While passive dosimeters have traditionally been used, the trend in radiation protection is increasingly toward the use of active personal dosimeters [19];
- Area-monitoring dosimeters, used to detect radiations in a selected area.

Although the use of dosimeters in estimation is very widespread, it leads to some problems. First, surveys have shown that dosimeters are not always properly used [20] or well-calibrated [21]. Moreover, even when properly used, these devices do not cover the entire body and are therefore subject to phenomena that may reduce their effectiveness. For example, the estimation provided by personal dosimeters is subject to the self-shielding effect of the body, especially when the rays come from behind. On the other hand, estimation methods based on area monitoring usually assume that a person remains in place, which of course is not always the case for people in a working environment.

Finally, it should be noted that all dosimeters register cumulative doses, which may correspond to a high exposure over a short period of time or a low exposure over a longer period of time, but these have different effects on the body.

3. Segmenting Human Models with MeshCNN

MeshCNN [22] is a convolutional neural network architecture specifically designed for analyzing 3D triangular meshes. Unlike traditional CNNs operating on grid-structured data, MeshCNN applies convolution and pooling directly to mesh edges, making it particularly suited for tasks such as segmentation and classification on irregular 3D geometries.

Figure 1: Edge-collapse operation in MeshCNN

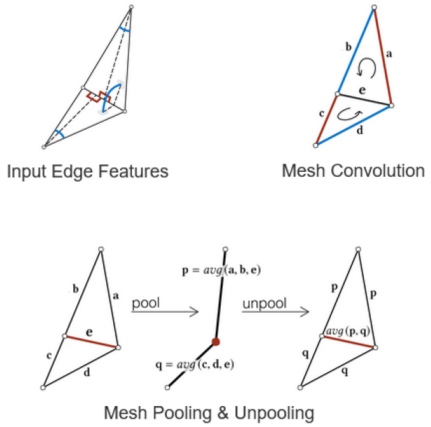

Edges are characterized by geometric features including the dihedral angle between adjacent faces, internal face angles, and normalized edge lengths. Mesh convolutions operate on an edge and its neighboring edges across adjacent triangles, extracting local geometric patterns. Downsampling is achieved via edge collapse operations, reducing mesh complexity while preserving important features. Unpooling layers restore the original resolution for segmentation tasks, as illustrated in Figure 1.

For our purposes, we leveraged pre-trained weights made available by the MeshCNN authors, trained on human body meshes segmented into eight anatomical regions [23]. The training dataset comprises 370 human models from the SCAPE [24], FAUST [25], and MIT [26] datasets, segmented according to the conventions in [27].

Our dataset consisted of two human models — one male[1] and one female[2] — processed via Blender[3] to match the required number of edges (approximately 2250) for MeshCNN input compatibility. The segmentation results

[1] https://free3d.com/3d-model/base-mesh-ready-to-be-rigged-15483.html
[2] https://sketchfab.com/3d-models/study-human-female-sculpt-854fbf358991477aab518e07556da906
[3] https://www.blender.org/

Figure 2: Segmentation obtained with MeshCNN for the two chosen models

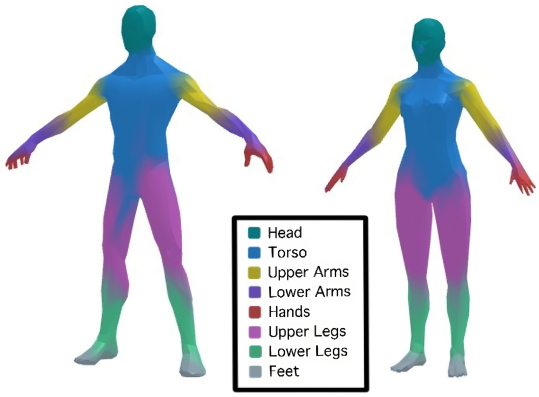

are depicted in Figure 2, with each anatomical region labeled and color-coded accordingly.

This segmentation enables the calculation of organ-specific effective doses based on which body parts are impacted by radiation in the simulation.

4. Creating 3D Scenes

The first step in our system involves constructing realistic 3D scenes that represent potential radiation exposure environments. For this purpose, we used the `trimesh` Python library [28], which provides efficient tools for manipulating and rendering triangular meshes.

Each scene is composed of three primary elements:

- **Radiation Source**: Modeled as a point source with configurable position and emitted intensity.
- **Human Model**: Selected from the segmented male or female meshes described previously, placed at a user-defined location within the scene.
- **Environmental Objects**: A configurable set of objects such as pillars, tables, or shields, each characterized by its position, size, and material properties (e.g., attenuation coefficients).

Figure 3 shows examples of two constructed scenes. In the first (a), a single massive pillar stands between the radiation source and the human figure, while the second (b) depicts a more complex setting involving a table assembled from multiple primitives.

Scene complexity can significantly influence radiation propagation, with factors such as object shape, size, material composition, and spatial arrangement playing key roles. Therefore, our framework allows flexible scene generation to evaluate a wide range of shielding scenarios and their effects on radiation dose distribution.

Figure 3: Two scenes built using the trimesh library, including a radioactive source, a human body and some objects partially blocking the rays

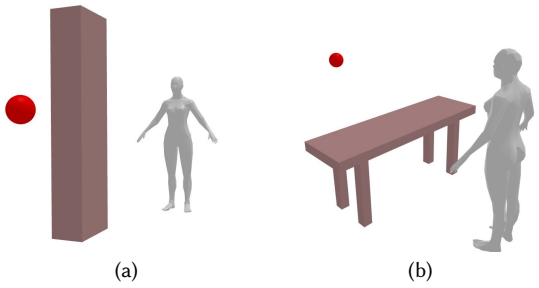

(a) (b)

In the subsequent simulations, different human positions and environmental objects were systematically varied to study their impact on effective dose estimation.

5. Modeling Radiation Exposure

To simulate the propagation of radiation within the constructed scenes, we developed a ray tracing algorithm tailored to radiological modeling. Unlike traditional ray tracing used in computer graphics for visual rendering, our method focuses on modeling energy deposition and attenuation due to interaction with materials.

5.1. Ray Tracing Methodology

The radiation source emits a large number of rays uniformly distributed in space. Each ray propagates until it either exits the scene or is absorbed by an object. For each ray, intersections with scene elements are detected using `trimesh` ray-mesh intersection routines.

If a ray strikes the human mesh, the intersected triangle is identified, allowing assignment of the absorbed dose to a specific anatomical region. If a ray encounters an object, the radiation intensity is attenuated according to the material properties before continuing propagation. For simplicity, scattering phenomena were neglected in this implementation. Figure 4 illustrates an example of rays propagating through a scene with a human model and environmental objects.

5.2. Radiation Intensity Attenuation

The radiation energy carried by each ray diminishes due to two mechanisms:

Figure 4: Rays created with a ray tracing algorithm. For demonstration purposes, the rays have been discretized with less accuracy

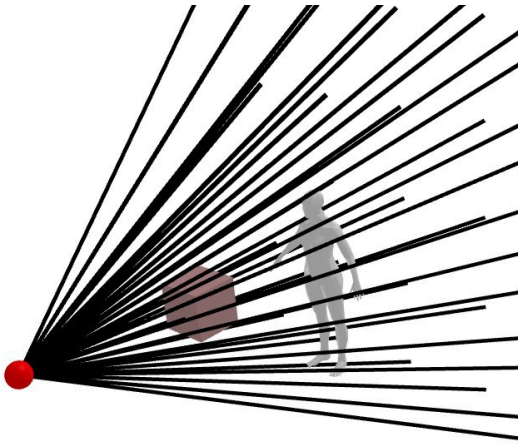

5.2.1. Distance Decay

The intensity decreases with the square of the distance from the source, following the inverse square law:

$$I = \frac{I_0}{r^2}$$

where I_0 is the source intensity and r is the distance traveled.

5.2.2. Material Attenuation

When a ray passes through an object, its intensity is reduced according to the Lambert–Beer law:

$$I = I_0 \cdot e^{-\mu x}$$

where μ is the linear attenuation coefficient of the material and x is the thickness traversed. Attenuation coefficients were obtained from the NIST database [29] for relevant materials.

5.3. Calculating the Effective Dose

To compute the effective dose:

1. For each human body part, the energy deposited by rays intersecting that region is accumulated.
2. The absorbed dose (in Gy) is computed based on deposited energy and local mass.
3. A radiation weighting factor ($w_R = 1$) is applied, appropriate for gamma and X-ray radiation.

Table 1
Tissue weighting factors according to ICRP 103 (ICRP 2007)[30]

Tissue	Tissue weighting factor
Bone-marrow (red), colon, lung, stomach, breast	0.12
Gonads	0.08
Bladder, oesophagus, liver, thyroid	0.04
Bone surface, brain, salivary glands, skin	0.01

4. Tissue weighting factors (w_T) specified by ICRP 103 [31] are used to adjust contributions from different body regions, reflecting their varying radiosensitivity (see Table 1).

Table 2
Percentage of red bone-marrow in the segmented parts

	Adult >25 years
Head	8%
Torso	82%
Upper Arms	3%
Lower Arms	0%
Hands	0%
Upper Legs	7%
Lower Legs	0%
Feet	0%

Table 3
Percentage of total skeletal mass contributed by segmented parts

	Adult Male	Adult Female
Head	14%	16%
Torso	33%	34%
Upper Arms	7%	6%
Lower Arms	5%	4%
Hands	2%	2%
Upper Legs	19%	19%
Lower Legs	14%	13%
Feet	6%	6%

For tissues such as bone marrow, bone surface, and skin that are distributed across multiple anatomical parts, weighting adjustments are made based on literature-reported fractional distributions [32, 30, 33] (see Tables 2, 3, and 4).

Thus, the final effective dose is a weighted sum of contributions from all body regions, accurately reflecting both spatial and biological factors influencing radiation risk.

Table 4
Percentage of skin surface in the segmented parts

	Adult
Head	9%
Torso	32%
Upper Arms	8%
Lower Arms	6%
Hands	5%
Upper Legs	19%
Lower Legs	14%
Feet	7%

6. Results

To validate our system, we designed a series of 3D scenes involving different human models (male and female), shielding objects, and materials. Radiation propagation and effective dose were computed for each configuration, allowing analysis of shielding effectiveness and the impact of spatial arrangement.

For all experiments, we used three common materials with known linear attenuation coefficients, summarized in Table 5.

Table 5
Linear attenuation coefficients for selected materials.

Material	Linear Attenuation Coefficient [cm^{-1}]
Plexiglass	0.0436
Particleboard	0.194
Concrete	0.960

6.1. Effect of Different Shielding Materials

We first evaluated the effectiveness of different materials in shielding radiation. In these experiments, a cubic object was placed in front of the torso of the human model. Figures 5a–f visualize the absorbed dose distribution for each configuration.

The numerical results, reported in Tables 6, 7, and 8, show that:

- Plexiglass provides limited shielding, resulting in high total absorbed doses.
- Particleboard achieves moderate reduction in absorbed dose.
- Concrete demonstrates superior shielding, reducing the absorbed dose to approximately one-third of that without any shielding.

In all cases, unprotected regions such as the head and arms still absorb considerable radiation, highlighting the importance of whole-body analysis.

Figure 5: Visualization of absorbed dose for different shielding materials. Redder areas indicate higher radiation exposure.

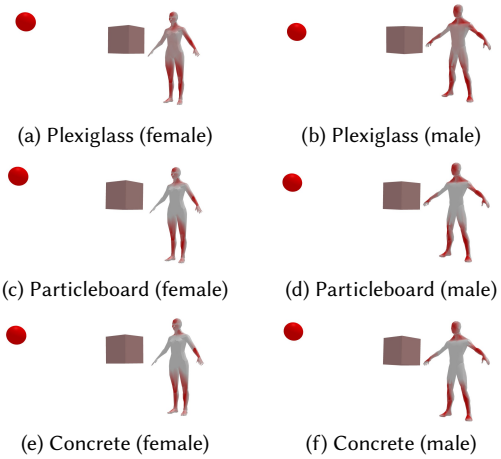

(a) Plexiglass (female) (b) Plexiglass (male)

(c) Particleboard (female) (d) Particleboard (male)

(e) Concrete (female) (f) Concrete (male)

Table 6
Effective dose (mSv) with Plexiglass shielding.

Body Part	Male	Female
Head	0.385	0.344
Torso	6.778	6.265
Upper Arms	0.014	0.012
Lower Arms	0.005	0.002
Hands	0.001	0.001
Upper Legs	0.131	0.146
Lower Legs	0.022	0.018
Feet	0.004	0.003
Total	**7.344**	**6.796**

6.2. Self-Shielding and Body Orientation Effects

Next, we investigated how body orientation relative to the radiation source affects exposure through self-shielding mechanisms. In one configuration, the human model faced the source directly; in the other, it was turned sideways.

Figures 6a–d depict the absorbed dose distributions for these two configurations. Numerical results are shown in Tables 9 and 10.

As expected, the torso absorbed the highest dose when facing the source. In the side-facing configuration, total absorbed dose was reduced by approximately 50%, demonstrating the significant protective effect of body

Table 7
Effective dose (mSv) with Particleboard shielding.

Body Part	Male	Female
Head	0.385	0.344
Torso	2.940	2.496
Upper Arms	0.008	0.003
Lower Arms	0.005	0.002
Hands	0.001	0.001
Upper Legs	0.088	0.095
Lower Legs	0.022	0.018
Feet	0.004	0.003
Total	**3.456**	**2.965**

Table 8
Effective dose (mSv) with Concrete shielding.

Body Part	Male	Female
Head	0.385	0.344
Torso	2.224	1.967
Upper Arms	0.006	0.0008
Lower Arms	0.005	0.001
Hands	0.001	0.0009
Upper Legs	0.078	0.085
Lower Legs	0.022	0.018
Feet	0.004	0.003
Total	**2.728**	**2.423**

positioning.

Table 9
Total effective dose (mSv) for male model under different orientations.

Orientation	Front-facing	Side-facing
Total Dose	22.026 mSv	10.851 mSv

Table 10
Total effective dose (mSv) for female model under different orientations.

Orientation	Front-facing	Side-facing
Total Dose	22.372 mSv	12.228 mSv

Figure 6: Effect of body orientation on radiation absorption.

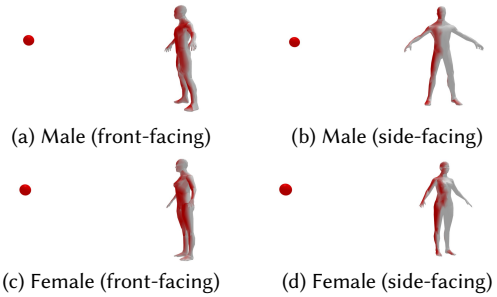

(a) Male (front-facing) (b) Male (side-facing)

(c) Female (front-facing) (d) Female (side-facing)

6.3. Shielding by Complex Objects

Finally, we evaluated scenarios involving more complex shielding, such as a dining table modeled using multiple primitives. Figure 7 illustrates this setup.

The results (Table 11) demonstrate how lower limbs and parts of the torso were partially shielded, significantly altering the absorbed dose distribution compared to the unshielded case.

Figure 7: Example of complex shielding scenario with a dining table.

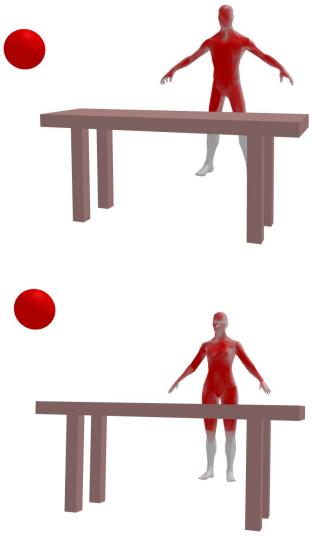

Table 11
Effective dose (mSv) in the dining table scenario.

Body Part	Male	Female
Total Dose	21.970 mSv	22.322 mSv

7. Conclusion and Future Work

In this work, we developed a system for estimating effective radiation dose absorbed by a human body placed within a 3D environment containing a radioactive source and various shielding objects. By integrating ray tracing techniques with 3D modeling and human body segmentation via MeshCNN, our method allows for spatially resolved and organ-specific dose calculations, taking into account both distance-based attenuation and material-dependent shielding effects.

Experimental results demonstrate the ability of the system to capture important phenomena such as self-shielding, differential material absorption, and the influence of complex object geometries on dose distribution. Comparative analyses across different shielding materials and body orientations underline the importance of detailed scene modeling for accurate radiation protection assessments. Overall, this work represents a step toward more comprehensive, flexible, and accurate tools for radiation exposure assessment, with potential applications in healthcare worker protection, medical imaging facility design, and radiological emergency response planning.

Declaration on Generative AI

During the preparation of this work, the authors used ChatGPT, Grammarly in order to: Grammar and spelling check, Paraphrase and reword. After using this tool/service, the authors reviewed and edited the content as needed and take full responsibility for the publication's content.

References

[1] United Nations Scientific Committee on the Effects of Atomic Radiation, UNSCEAR 2020/2021 Report Volume I: "Sources, effects and risks of ionizing radiation"; Annex A: "Evaluation of medical exposure to ionizing radiation", https://www.unscear.org/unscear/en/publications/2020_2021_1.html, 2021.

[2] F. A. Mettler, M. Mahesh, M. Bhargavan-Chatfield, C. E. Chambers, J. G. Elee, D. P. Frush, D. L. Miller, H. D. Royal, M. T. Milano, D. C. Spelic, A. J. Ansari, W. E. Bolch, G. M. Guebert, R. H. Sherrier, J. M. Smith, R. J. Vetter, Patient exposure from radiologic and nuclear medicine procedures in the united states: Procedure volume and effective dose for the period 2006–2016, Radiology 295 (2020) 418–427. doi:10.1148/radiol.2020192256, pMID: 32181730.

[3] J. Hausleiter, T. Meyer, F. Hermann, M. Hadamitzky, M. Krebs, T. C. Gerber, C. McCollough, S. Martinoff, A. Kastrati, A. Schömig, S. Achenbach, Estimated Radiation Dose Associated With Cardiac CT Angiography, JAMA 301 (2009) 500–507. URL: https://doi.org/10.1001/jama.2009.54. doi:10.1001/jama.2009.54.

[4] M. Woźniak, D. Połap, R. K. Nowicki, C. Napoli, G. Pappalardo, E. Tramontana, Novel approach toward medical signals classifier, in: Proceedings of the International Joint Conference on Neural Networks, volume 2015-September, 2015. doi:10.1109/IJCNN.2015.7280556.

[5] M. Wozniak, D. Polap, L. Kosmider, C. Napoli, E. Tramontana, A novel approach toward x-ray images classifier, in: Proceedings - 2015 IEEE Symposium Series on Computational Intelligence, SSCI 2015, 2015, p. 1635 – 1641. doi:10.1109/SSCI.2015.230.

[6] P. Andreo, Monte carlo techniques in medical radiation physics, Physics in Medicine & Biology 36 (1991) 861. URL: https://dx.doi.org/10.1088/0031-9155/36/7/001. doi:10.1088/0031-9155/36/7/001.

[7] C. Napoli, C. Napoli, V. Ponzi, A. Puglisi, S. Russo, I. E. Tibermacine, Exploiting robots as healthcare resources for epidemics management and support caregivers, in: CEUR Workshop Proceedings, volume 3686, 2024, p. 1 – 10.

[8] A. L. Fielding, Monte-carlo techniques for radiotherapy applications i: introduction and overview of the different monte-carlo codes, Journal of Radiotherapy in Practice 22 (2023) e80. doi:10.1017/S1460396923000079.

[9] N. Boutarfaia, S. Russo, A. Tibermacine, I. E. Tibermacine, Deep learning for eeg-based motor imagery classification: Towards enhanced human-machine interaction and assistive robotics, in: CEUR Workshop Proceedings, volume 3695, 2023, p. 68 – 74.

[10] H. Park, H. Paganetti, J. Schuemann, X. Jia, C. H. Min, Monte carlo methods for device simulations in radiation therapy, Physics in Medicine & Biology 66 (2021) 18TR01. URL: https://dx.doi.org/10.1088/1361-6560/ac1d1f. doi:10.1088/1361-6560/ac1d1f.

[11] C. M. C. Ma, I. J. Chetty, J. Deng, B. Faddegon, S. B. Jiang, J. Li, J. Seuntjens, J. V. Siebers, E. Traneus, Beam modeling and beam model commissioning for monte carlo dose calculation-based radiation therapy treatment planning: Report of aapm task group 157, Medical Physics 47 (2020) e1–e18. doi:https://doi.org/10.1002/mp.13898.

[12] S. Russo, I. E. Tibermacine, A. Tibermacine, D. Chebana, A. Nahili, J. Starczewscki, C. Napoli, Analyzing eeg patterns in young adults exposed to different acrophobia levels: a vr study, Frontiers in Human Neuroscience 18 (2024). doi:10.3389/fnhum.2024.1348154.

[13] S. Russo, C. Napoli, A comprehensive solution for psychological treatment and therapeutic path planning based on knowledge base and expertise sharing, in: CEUR Workshop Proceedings, volume 2472, 2019, p. 41 – 47.

[14] C. Kontaxis, G. H. Bol, J. J. W. Lagendijk, B. W. Raaymakers, Deepdose: Towards a fast dose calculation engine for radiation therapy using deep learning, Physics in Medicine & Biology 65 (2020) 075013. URL: https://dx.doi.org/10.1088/1361-6560/ab7630. doi:10.1088/1361-6560/ab7630.

[15] N. Brandizzi, A. Fanti, R. Gallotta, S. Russo, L. Iocchi, D. Nardi, C. Napoli, Unsupervised pose estimation by means of an innovative vision transformer, in: Lecture Notes in Computer Science (including subseries Lecture Notes in Artificial Intelligence and Lecture Notes in Bioinformatics), volume 13589 LNAI, 2023, p. 3 – 20. doi:10.1007/978-3-031-23480-4_1.

[16] T. I. Götz, C. Schmidkonz, S. Chen, S. Al-Baddai, T. Kuwert, E. W. Lang, A deep learning approach to radiation dose estimation, Physics in Medicine & Biology 65 (2020) 035007. URL: https://dx.doi.org/10.1088/1361-6560/ab65dc. doi:10.1088/1361-6560/ab65dc.

[17] United Nations Scientific Committee on the Effects of Atomic Radiation, UNSCEAR 2020/2021 Report Volume I: "Sources, effects and risks of ionizing radiation"; Annex D: "Evaluation of occupational exposure to ionizing radiation", https://www.unscear.org/unscear/en/publications/2020_2021_4.html, 2021.

[18] A. Abaza, New trend in radiation dosimeters, American Journal of Modern Physics 7 (2018) 21. doi:10.11648/j.ajmp.20180701.13.

[19] T. Bolognese-Milsztajn, M. Ginjaume, F. Vanhavere, Active Methods & Instruments for Personal Dosimetry of External Radiation: Present Situation in Europe and Future Needs, EDP Sciences, Les Ulis, 2004, pp. 65–82. URL: https://doi.org/10.1051/978-2-7598-0117-6.c008. doi:doi:10.1051/978-2-7598-0117-6.c008.

[20] R. M. Sánchez, E. Vano, J. M. Fernández, F. Rosales, J. Sotil, F. Carrera, M. A. García, M. M. Soler, J. Hernández-Armas, L. C. Martínez, J. F. Verdú, Staff doses in interventional radiology: A national survey, Journal of Vascular and Interventional Radiology 23 (2012) 1496–1501. URL: https://www.sciencedirect.com/science/article/pii/S105104431200591X. doi:https://doi.org/10.1016/j.jvir.2012.05.056.

[21] O. Ciraj-Bjelac, E. Carinou, F. Vanhavere, Use of active personal dosimeters in hospitals: Eurados survey, Journal of Radiological Protection 38 (2018) 702. URL: https://dx.doi.org/10.1088/1361-6498/aabce1. doi:10.1088/1361-6498/aabce1.

[22] R. Hanocka, A. Hertz, N. Fish, R. Giryes, S. Fleishman, D. Cohen-Or, Meshcnn: A network with an edge, ACM Transactions on Graphics (TOG) 38 (2019) 90:1–90:12.

[23] H. Maron, M. Galun, N. Aigerman, M. Trope, N. Dym, E. Yumer, V. Kim, Y. Lipman, Convolutional neural networks on surfaces via seamless toric covers 36 (2017). doi:10.1145/3072959.3073616, publisher Copyright: © 2017 ACM.; ACM SIGGRAPH 2017 ; Conference date: 30-07-2017 Through 03-08-2017.

[24] D. Anguelov, P. Srinivasan, D. Koller, S. Thrun, J. Rodgers, J. Davis, Scape: Shape completion and animation of people, ACM Transactions on Graphics (TOG) 24 (2005) 408–416. doi:10.1145/1073204.1073207.

[25] F. Bogo, J. Romero, M. Loper, M. J. Black, FAUST: Dataset and evaluation for 3D mesh registration, in: Proceedings IEEE Conf. on Computer Vision and Pattern Recognition (CVPR), Columbus, Ohio, USA, 2014, pp. 3794 –3801. doi:10.1109/CVPR.2014.491.

[26] D. Vlasic, I. Baran, W. Matusik, J. Popović, Articulated mesh animation from multi-view silhouettes, ACM Trans. Graph. 27 (2008) 1–9. URL: https://doi.org/10.1145/1360612.1360696. doi:10.1145/1360612.1360696.

[27] E. Kalogerakis, A. Hertzmann, K. Singh, Learning 3d mesh segmentation and labeling 29 (2010). URL: https://doi.org/10.1145/1778765.1778839. doi:10.1145/1778765.1778839.

[28] Dawson-Haggerty et al., trimesh (version 3.2.0), 2019.

[29] J. Hubbell, S. Seltzer, Tables of x-ray mass attenuation coefficients and mass energy-absorption coefficients 1 kev to 20 mev for elements z = 1 to 92 and 48 additional substances of dosimetric interest, 1995.

[30] ICRP, Basic anatomical and physiological data for use in radiological protection reference values, ICRP Publication 89. Ann. ICRP 32 (2002).

[31] ICRP, The 2007 recommendations of the international commission on radiological protection, ICRP Publication 103. Ann. ICRP 37 (2007).

[32] M. Cristy, Active bone marrow distribution as a function of age in humans., Physics in medicine and biology 26 3 (1981) 389–400.

[33] C. C. Lund, N. C. Browder, The estimation of areas of burns, Surg Gynecol Obste 79 (1944) 352–358.